FULL PAPER

Biomineralization

**ADVANCED
MATERIALS
INTERFACES**

www.advmatinterfaces.de

Biomineralization at Titanium Revealed by Correlative 4D Tomographic and Spectroscopic Methods

Xiaoyue Wang, Brian Langelier, Furqan A. Shah, Andreas Korinek, Matthieu Bugnet, Adam P. Hitchcock, Anders Palmquist, and Kathryn Grandfield*

At an implant biointerface, where an engineered material merges into a biological environment, complex biophysicochemical interactions occur. One typical biointerface is the bond between human bone and dental or orthopedic implants, which is based on the biomineralization of essential bone components such as hydroxyapatite, at the implant surface. However, the exact bonding mechanism between bone and implants is still unclear. The distribution of both the mineralized and organic components of bone at the interface, and their origins, requires improved characterization. Here, the first correlative characterization is reported using multiple-length-scale tomography and spectroscopy techniques to probe the chemical structure of the biointerface between human bone and commercial titanium dental implant down to the atomic scale in four dimensions (4D). The existence of an intervening transition zone bonding mature bone tissue is demonstrated to implant at multiple length scales, where the phase of bone mineral differs immediately adjacent to the implant and atomic-scale osseointegration is confirmed. The correlative 4D electron energy loss spectroscopy tomography and atom probe tomography workflow established herein is transferable to other applications in materials or biological sciences.

1. Introduction

Biominerals are abundant natural materials formed from the interaction of organic and inorganic components mediated by living organisms.[1] Their intricate hierarchical structure and distinctive mechanical properties have attracted interest to unveil their formation mechanisms, as these mechanisms could form the basis for model systems for the design and synthesis of biomimetic materials.[2] Calcium phosphates (CaP) are one of the most highly researched classes of biominerals since the carbonated apatite crystal is the building block of both bones and teeth of vertebrates, and consequently, they have extensive biomedical applications.[3] The mechanism of CaP mineralization in bone is not fully understood. A transient phase of amorphous calcium phosphate (ACP),[4] and the mediating roles of collagen[5] and noncollagenous proteins[6] have been reported from both in vivo and in vitro studies. Bone regeneration and remodeling play a key role in the maintenance of healthy bone quality, for example in repairing naturally occurring microfractures, maintaining ionic balance, and enabling the interlocking of living bone tissue to artificially synthesized biomaterial surfaces, that is, in the case of dental or orthopedic implants. Every year, millions of dental implants, hip and knee replacements, prosthesis, and even 3D-printed customized bone implants are placed in human bodies.[7] One key to the success of these dental and orthopedic surgeries is whether mineralized bone is able to form at these artificial interfaces to form a long-lasting and biomechanically load-bearing bond, termed osseointegration.[8,9] The research on osseointegration not only explores the strategies of bone-implant design and modification to accelerate bone regeneration,[10] but also helps to shed light on the mechanism of biomineralization at these interfaces between natural organisms and engineered biomaterials.

However, the mechanism of osseointegration is still debated. Physicomechanical interdigitation and biochemical bonding have been reported as the potential contact modes at bone–implant interfaces.[11] Davies et al. proposed a noncollagenous hypermineralized layer similar to the cement line as the layer responsible for direct bonding of bone and implant.[12,13] Steflik et al. observed the existence of proteoglycans at the

Dr. X. Y. Wang, Prof. K. Grandfield
Department of Materials Science and Engineering
McMaster University
Hamilton L8S 4L7, Canada
E-mail: kgrandfield@mcmaster.ca

Dr. B. Langelier, Dr. A. Korinek
Canadian Centre for Electron Microscopy
McMaster University
Hamilton L8S 4L7, Canada

Dr. F. A. Shah, Prof. A. Palmquist
Department of Biomaterials
Sahlgrenska Academy at University of Gothenburg
Göteborg 405 30, Sweden

Prof. M. Bugnet
University of Lyon
INSA Lyon
UCBL Lyon 1
MATEIS
UMR 5510 CNRS
Villeurbanne Cedex 69621, France

Prof. A. P. Hitchcock
Department of Chemistry and Chemical Biology
McMaster University
Hamilton L8S 4M1, Canada

**ADVANCED
SCIENCE NEWS**
www.advancedsciencenews.com

**ADVANCED
MATERIALS
INTERFACES**
www.advmatinterfaces.de

interface which are highly polyanionic and able to bind Ca^{2+} by electrostatic bonding so as to generate an initial amorphous Ca-rich layer.[14,15] McKee and Nanci showed that osteopontin in cement lines acts as an interfacial adhesion promoter in bone–bone bonding and bone–implant bonding.[16] In addition, an osseohybridization model was recently put forward suggesting the potential presence of a $CaTiO_3$ hybridized layer at the titanium dental implant–bone interface.[17] One of the key remaining issues is the distribution of calcium-based (i.e., inorganic) and carbon-based (i.e., organic) components, at the bone–implant interface and their origins. Until now, this has not been fully understood, particularly with spatial and chemical clarity at the nanometer scale.

Owing to the hierarchically structured nature of bone and the inhomogeneous topographical quality of the implant surface, multiple-length-scale 3D visualization characterization techniques have been exploited to visualize bone–implant interfaces.[7] The understanding of osseointegration has also evolved with breakthroughs in discerning finer structures at the interface. X-ray microcomputed tomography (X-ray CT) enables visualization of large volumes with micrometer resolution to reveal microscaled bone ingrowth surrounding the implant for histological-like quantitative analysis.[18] The concept of nano-osseointegration was put forward based on electron tomography (ET) observations with scanning transmission electron microscopy (STEM) high-angle annular dark-field (HAADF) imaging mode that enhanced compositional contrast.[19] Recently, the atomic continuity at the bone-implant interface was also investigated by atom probe tomography (APT).[20,21] However, in order to contribute to the unresolved mechanisms of osseointegration, both nanoscale structural and elemental distribution at the bone–implant interface is needed across three dimensions. Thus, spatial 3D characterization techniques should step further toward so-called 4D techniques by adding chemical information as the fourth dimension.[22]

Spectroscopic electron tomography is a recently developed 4D technique to visualize 3D chemical information with nanometer resolution.[23] Based on acquiring energy-filtered images or spectroscopic images at different tilt angles, it comprises either energy-filtered transmission electron microscopy (TEM) tomography, or more recently energy-dispersive X-ray spectroscopy tomography, or electron energy-loss spectroscopy (EELS) tomography in STEM mode.[24] With the development of detector technology, EELS tomography is able to limit the electron beam dose exposure to biological specimens and has high sensitivity to light elements.[25] APT, another 4D imaging technique, is based on field emission of surface atoms under a strong electric field or pulsed UV laser illumination. APT combines subnanometer spatial resolution with chemical sensitivity across the entire periodic table.[26,27] APT has been successfully applied to study biomaterials, such as biominerals,[28,29] dentin,[30] and human bone.[31] X-ray absorption spectroscopy (XAS) in soft X-ray scanning transmission X-ray microscopes (STXMs) provides speciation-based chemical mapping in 2D[32] and 3D[33] with better than 30 nm spatial resolution and has been applied to several biomineralization systems,[34,35] including bone.[36] Furthermore, STEM-EELS and STXM-XAS are able to probe the chemical states of each element at the nanoscale on the basis of characteristic fine structural features

at the core level excitation edge. However, considering the complex nature of biomaterials and the limitations of each single technique, correlative characterization using complementary techniques is essential for reliable analysis and validation.[37–39]

Here, we report the first correlative application of on-axis ET, EELS tomography, and APT, as well as complementary electron energy-loss near-edge structure (ELNES), and STXM-XAS to acquire nanoscaled structural and chemical information from the intricate biointerface between human bone and titanium dental implant to provide insights on bone attachment mechanisms.

2. Results and Discussion

2.1. Osseointegration on Multiple Length Scales

Human bone has complex hierarchical structures with nanoscaled building units of type I collagen and carbonated hydroxyapatite crystals. After a titanium implant is placed in vivo, new bone forms along the implant surface to generate a biomechanically functional integration. Due to the hierarchical character of bone, this integration should also exist on multiple length scales. As revealed in **Figure 1**, correlative tomographic reconstructions of the same sample sharpened into a needle can be used to visualize the human bone–implant interface from nanometer to atomic length scales. Figure 1a shows the reconstructed 3D volume from on-axis HAADF-STEM ET, which provides Z- (atomic number) contrast to differentiate the Ti implant (the brightest structure), collagen fibrils (the darkest structure), and apatite (the intermediate contrast
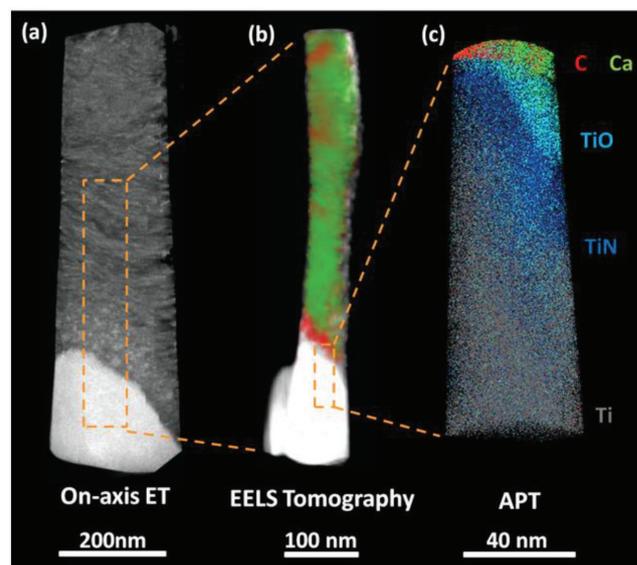

Figure 1. Correlative tomographic reconstructions of the human bone–implant interface from the same sample needle. a) On-axis electron tomographic reconstruction of the bone (top)–implant (bottom) interface with 3D renderings in gray scale. b) A representative 3D on-axis EELS volume, where red represents carbon (C), green represents calcium (Ca), and white represents titanium (Ti). c) Atom probe tomography 3D reconstruction with Ca-containing ions displayed in green, C-containing ions in red, TiO ions in bright blue, TiN ions in dark blue, and Ti ions in gray.

**ADVANCED
SCIENCE NEWS**

www.advancedsciencenews.com

**ADVANCED
MATERIALS
INTERFACES**

www.advmatinterfaces.de

flake-like structures).[40] The continuous incorporation of bone structure with the nanotopographic oxide layer on the surface of this laser-modified commercially pure titanium (cp-Ti) dental implant is visualized in 3D, providing experimental evidence of nano-osseointegration. Since this implant has been placed in the human body for 47 months, the bone near the interface has likely been remodeled and the ultrastructure of mature bone can be identified in orthoslices of the reconstructed volume (see Figure S1 and Video S1 in the Supporting Information). On-axis ET not only circumvents the "missing wedge" problem, which causes artifacts and limits the resolution of 3D reconstructions,[40] but it is also suitable to correlate with 4D EELS tomography (Figure 1b) and APT (Figure 1c) due to its needle-like sample geometry.

The EELS tomographic reconstruction (Figure 1b) of the same needle, after sharpening to 100 nm in diameter to enable spectroscopy, complements the nanoscale chemical distributions to the 3D structures at the interface. Even though the Z-contrast of HAADF imaging in ET helps to differentiate the different phases in the sample, the EELS elemental reconstructed volume offers more accurate chemical visualization. Ca-concentrated areas (in green), representing bone apatite, are distributed complementary to C-concentrated areas (in red), representing organic components of bone. For APT characterization, the same needle was further sharpened down to around 50 nm in diameter using focused ion beam (FIB). The 3D reconstructed APT volume (Figure 1c) is rendered in ions and both Ca and C were shown in direct contact with the oxide layer, suggesting osseointegration at the atomic level. This correlative tomography workflow helps to visualize the inhomogenous and hierarchical bone–implant interface, and it is also applicable to the investigation of other complex biointerphases.

2.2. Nanoscale Elemental Distribution in 3D

Based on the conflicting mechanisms of osseointegration, elucidating the elemental distribution at the bone–implant interface is a vital piece of experimental evidence. 2D EELS or EDX elemental mapping has been the gold standard to present elemental distribution at interfaces. However, these spectroscopic methods in TEM are based on 2D projections of a 3D sample, which are therefore difficult to interpret as many overlapping features in the sample volume are collapsed into 2D. EELS tomography enables visualization of elemental distribution in 3D reconstructed volumes, and much more clearly correlates the chemical information to the structures identified by HAADF STEM tomography than the granular and sparse 2D EELS maps. **Figure 2**a,b shows a comparison between 2D EELS elemental maps and EELS tomography reconstructions, respectively. Collagen fibrils, visualized as the higher contrast, highly C-concentrated areas, are clearly identified from the 3D EELS orthoslices (Figure 2c) as structures distributed parallel to the implant interface throughout the bone (highlighted in the yellow box), while other collagenous structures are more randomly distributed near the interface (highlighted in the red box). This morphology change could be described as a transitional layer, where bone structure is less ordered, with randomly distributed collagen fibrils and denser bone apatite
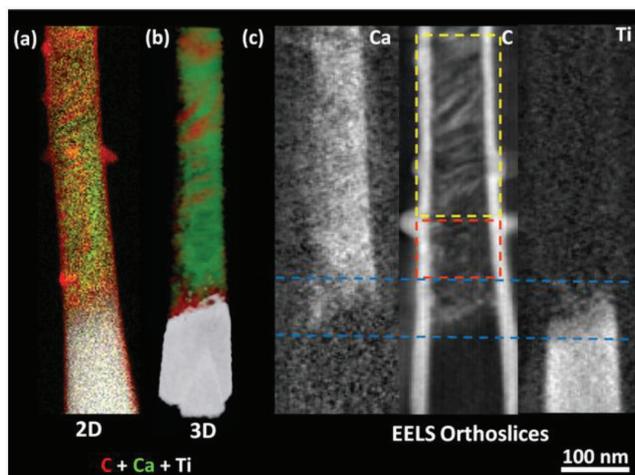

Figure 2. Representative elemental distribution of bone–implant interface revealed by on-axis EELS tomography. a) EELS elemental distribution 2D maps of C (red), Ca (green), and Ti (white) from the 0° tilt angle. b) The corresponding 3D reconstructed elemental volumes from EELS maps acquired over a tilt range of ±70°. c) XY orthoslices extracted from the 3D reconstructed EELS tomograms showing the elemental distribution of Ca, C, and Ti inside of the sample volume. The implant oxide layer is highlighted by blue lines, and the ordered collagen fibrils are highlighted by the yellow box, with an intermediary unorganized zone in red.

distribution directly at the oxide layer surface (see Figure S2 and Video S2 in the Supporting Information). The titanium oxide layer is highlighted by two blue dotted lines through the 3D EELS orthoslices (Figure 2c). Both C and Ca were observed penetrating this oxide layer, which correlates with our observations presented in Figure 1 from APT (elaborated in **Figure 3**), supporting an atomic-scale integration of bone constituents into the surface oxide.

Due to the considerable electron beam exposure during the EELS tomography acquisition, the effect of beam damage should be taken into consideration. A clear beam-induced hydrocarbon contamination shell was observed on the surface of the sample needle (Figure 2c). Since bone is an organic and inorganic composite material, it acts as a local source of hydrocarbons. Studies have proven that this thin C contamination layer covering the sample could act as a C coating to reduce mass loss.[41] By comparing EELS tomography with electron tomography, no obvious structural artifacts, besides the formation of the C shell, are seen. This C shell has been cropped from reconstructed volumes for easier visualization (Figure 2b).

2.3. Atomic Level Mapping of Osseointegration

Figure 3a shows another representative APT reconstruction of the interface between human bone and oxidized Ti implant. Both Ca, which represents bone mineral, and C, which represents organic components, are shown in direct contact with the oxide layer, corroborating the observations in our correlative EELS tomography and previous APT datasets mentioned above. A clear concentration gradient of elements Ca (representing bone) and Ti (implant) are noted at subnanometer length scales from the proxigram in Figure 3c,d. This provides
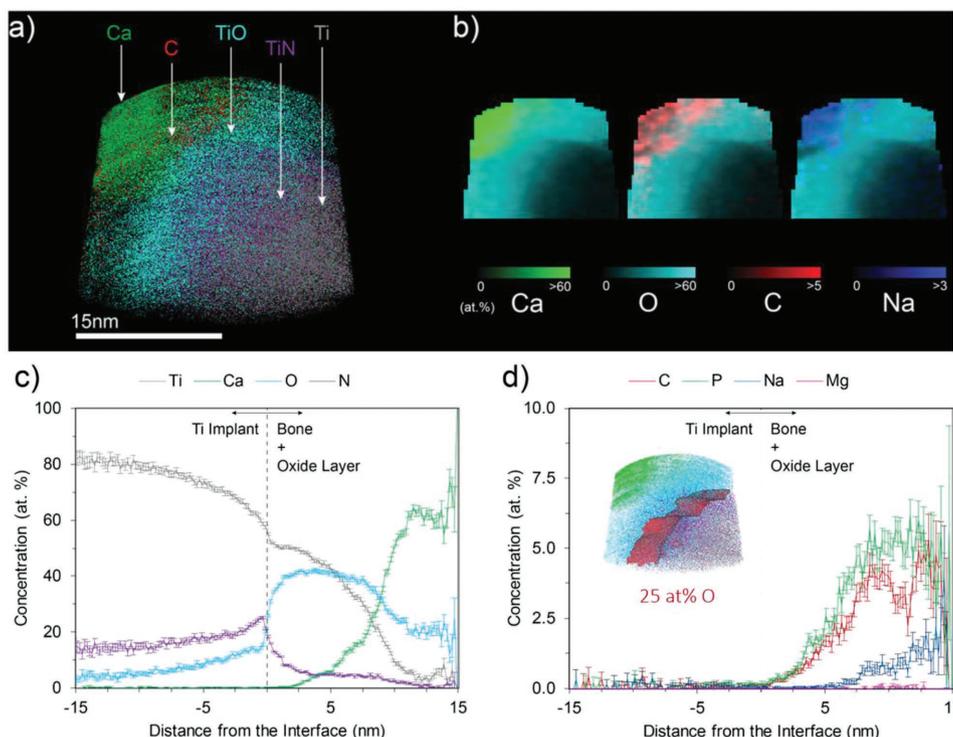
Figure 3. Atom probe tomography of the human bone–implant interface. a) 3D reconstructed APT volume with Ca-containing ions displayed in green, C-containing ions displayed in red, TiO ions displayed in bright blue/cyan, TiN ions in purple, and Ti ions displayed in gray. Atomic-scale integration of Ca ions with the oxide layer is noted. b) Overlay of Ca, C, and Na ion positions on oxygen concentration maps. c) Supporting proximity histograms across the implant–bone interface showing the integration of Ca within the oxide, and d) the presence of trace elements like Mg and Na in the bone structure which presents immediately adjacent to the oxide lay of the implant. The proxigram was set from the isosurface 25 at% O, which is shown in red in inset of panel (d).

evidence that osseointegration consists of an atomic-scale interphase. Other APT studies on different implant surfaces, such as mesoporous titania coatings[21] and a sand-blasted acid etched (SLA, Straumann)[20] also showed Ca immediately adjacent to titanium implant surfaces. In this work, a small N enrichment is noted between Ti metal and oxide layer, which may be attributed to the laser surface modification process carried out in ambient air. Although APT provides atomic-scale 3D visualization of element distributions, it is unable to determine the exact chemical environment of each element, which is complemented by a more detailed spectroscopic study in the following section. However, due to the high sensitivity of APT (down to 1 ppm), trace elements of magnesium (Mg) and sodium (Na) were detected at the interface. Note that due to overlaps between Na+ (23 Da) and Mg+ (24 Da) with peaks of Ti2+, identification of Na and Mg in bone is much easier than differentiating these elements in the interfacial layer where Ti is present. Previous APT research on human bone has demonstrated the colocalization of Na with C-rich regions in bone structure.[31] This result agrees well with observations from secondary ion mass spectroscopy, which stated that abundant Na exists largely in organic material in bone.[42] However, Na+ also plays a key function in ion exchange and transportation during cell activations involved in the bone generation process. Inorganic phosphate (Pi) is an essential component of bone mineral, which has been known to be accumulated and transported by sodium-dependent (NaPi) transporters in osteogenic cells.[43]

Also, a similar functional protein sodium-dependent citrate transporter is reported to regulate citrate take-up and release in osteoblasts.[44] Citrate has been reported to bind strongly on the surface of apatite to regulate crystal growth orientation and size.[45,46] Therefore, the presence of Na in bone is indeed complex and perhaps cannot be segregated simply into the organic and inorganic regions.

2.4. Transient Mineral Phase at Bone–Implant Interface

Hydroxyapatite or its carbonate-substituted form is generally accepted to be the inorganic constituent of bone, which, evidence suggests, passes through different apatite phase transitions during its mineralization process. Different apatite phases have significantly different Ca/P concentration ratios, and thus Ca/P ratio is a traditional method to differentiate apatite phases.[47] However, the atomic ratio determined by APT is quantitatively unreliable for such inhomogeneous composites. Due to the comparatively high background and thermal tails in the APT spectra, which are caused by the low thermal conductivity of the sample, many small peaks are obscured, thus reducing the accuracy of quantitative analysis. This is particularly important for quantification of P, as it has a tendency to form numerous complex ions when evaporating during the APT data acquisition stage.[31] However, ELNES can probe the local environment of Ca atoms so as to differentiate different apatite phases, combining superior
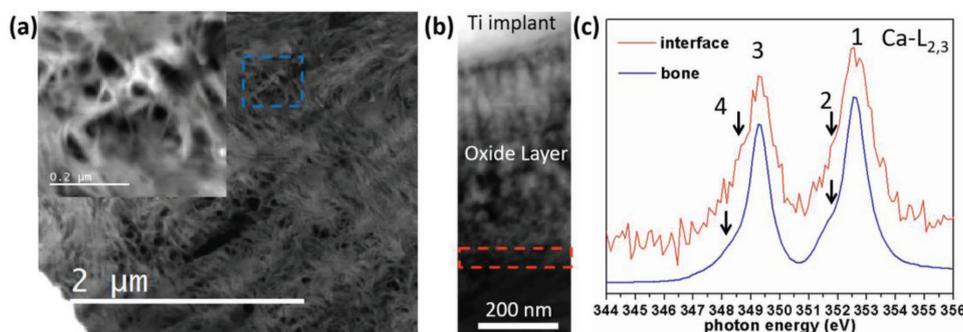
Figure 4. ELNES comparison of Ca-L$_{2,3}$ from bone and interface. HAADF-STEM images of a) mature bone and b) bone–implant interface, where the titanium oxide layer spans roughly 300 nm past the bright Ti substrate. c) Ca-L$_{2,3}$ edges of bone (in blue) and interface (in red) are extracted from the regions highlighted by the dashed squares in corresponding colors in panels (a) and (b). Four discernable peaks are indicated by arrows and their accurate positions are included in Table 1.

spatial resolution with high-energy resolution.[48] **Figure 4**c compares Ca-L$_{2,3}$ ELNES from bone (blue box in Figure 4a) and the bone–implant interface (red box in Figure 4b). The double peak spectrum can be deconvoluted into four components by Gaussian fitting (Figure S4, Supporting Information). While the two main spin–orbit split peaks L$_3$ (peak 3), and L$_2$ (peak 1) are positioned identically among different apatites, the positions of peaks 2 and 4 are characteristically used to identify the apatite phase.[49] The detailed peak positions of interest together with reference apatites are listed in **Table 1**.[49] A slight shift in peak 4 is discerned by comparing the Ca-L$_{2,3}$ ELNES of bone (Figure 4c, blue line) and the interface (Figure 4c, red line). Based on the comparison with reference apatites in Table 1, the Ca of bone should originate from hydroxyapatite (HA), whereas the Ca at the interface is similar to amorphous calcium apatite (ACP). ACP has been suggested as a transient phase during mineralization processes by many studies, for example, mouse tooth enamel[49] and zebrafish fin ray bone.[50] Here, the transient phase of ACP was observed displaying direct contact with the implant oxide layer at the human bone–implant biomineralization interface. The existence of a different Ca species at the interface is also supported by STXM-XANES of Ca-L$_{2,3}$ (Figure S5, Supporting Information).

2.5. TiN Layer in the Commercial Dental Implant

A distinct N-rich layer was observed between the oxide layer and Ti metal in the APT 3D reconstructed volume (**Figure 5**d). In order to identify the origin of N in this layer, the N-K edge was studied by STXM-XANES on a similar lamellar TEM

sample from the same specimen to gain a large-scale overview of the spatial distribution of N-containing species. The optical density difference map (Figure 5b) shows an obvious N-rich layer which is correlated to the APT results. From the STEM-HAADF (Figure 5a) and STXM (Figure 5b) images, this N-rich layer distributes perfectly along the interface. XANES spectra extracted from representative regions of the bone (green), N-rich layer (blue), and implant (red) (Figure 5e) were used to fit the N-K edge stack (images at 50 energies from 395 to 421 eV) to derive component maps of the three distinct N-containing species. These component maps are presented as a combined rescaled color-coded composite (Figure 5c). Spectroscopically, the narrow double peak around 400 eV in the N-K edge spectrum of the N-rich layer (blue in Figure 5) is the characteristic "fingerprint" of TiN.[51] The N-K edge spectrum of the implant region (red in Figure 5) has a completely different fine structure with only one sharp peak followed by a broad signal in the N-K continuum. The shape of the N-K edge spectrum of localized band in the implant region matches that of the hexagonal Ti$_2$N phase.[52] The implant used in this study is made from cp-Ti,[40] which has a hexagonal close-packed atomic structure. Nitrogen is soluble in the hexagonal structure to a limited extent.[53] The N-K edge spectrum of the bone region (green in Figure 5) is likely the mixture of signals from different organic components of bone,[48] such as collagen and other functional noncollagenous proteins. The fine structure in the 400–403 eV region is typical of N-K edge XANES of proteins, which are dominated by N 1s $\rightarrow \pi^*_{peptide}$ transitions.[54,55] The map of the bone component and a comparison to the N-K edge spectrum of collagen are shown in Figure S7 (Supporting Information).

In order to investigate whether this N-rich layer was formed in vivo, the same dental implant prior to implantation was characterized by EELS. A similar N-rich region was also discernible from the elemental mapping (Figure S6, Supporting Information), suggesting that, as suspected, it was formed during the laser modification of the implant surface in an ambient air environment. In other studies, a titanium hydride layer has been reported as a result of argon plasma treatment, sandblasting, and acid etching of titanium implant surfaces.[56,57] However, this is the first time that this N-rich layer localized on the subsurface of a
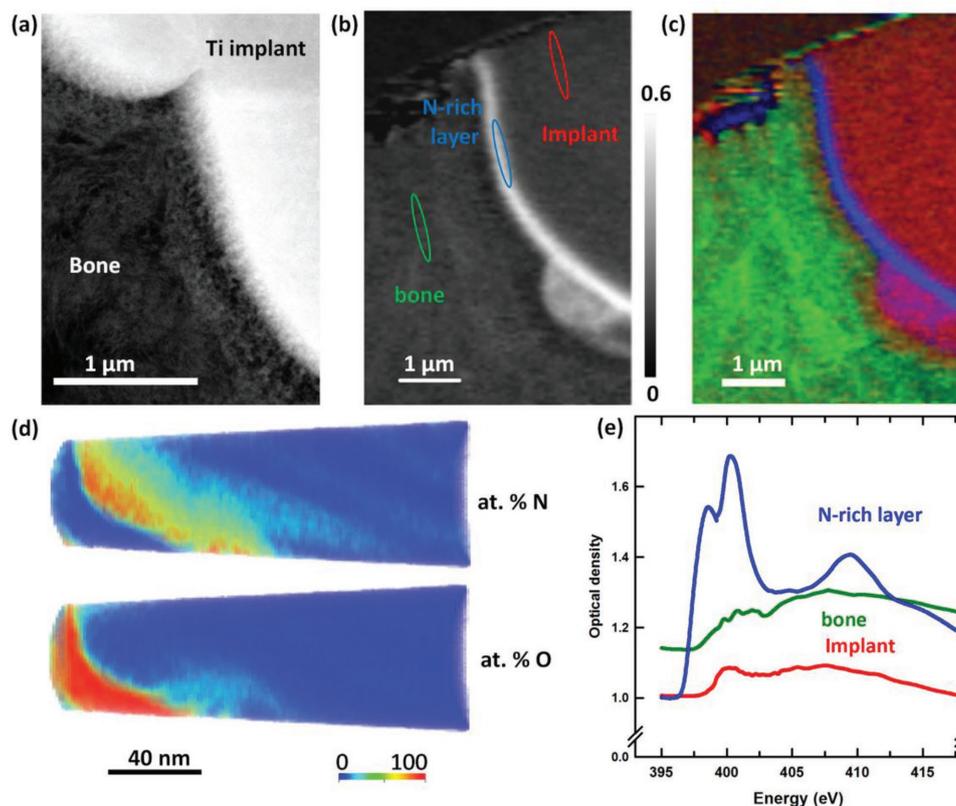
Table 1. Energy positions of four main peaks Ca-L$_{2,3}$ ELNES. The energy separation (Δ) of peaks 3 and 4 highlights the crystalline nature of the minerals.

	Peak 1 position [eV]	Peak 2 position [eV]	Peak 3 position [eV]	Peak 4 position [eV]	$\Delta_{peak3-peak4}$ [eV]
Reference HA	352.6	351.6	349.3	348.4	0.9
Reference ACP	352.6	351.6	349.3	348.8	0.5
Bone	352.6	351.6	349.3	348.4	0.9
Interface	352.6	351.6	349.3	348.7	0.6

**ADVANCED
SCIENCE NEWS**
www.advancedsciencenews.com

**ADVANCED
MATERIALS
INTERFACES**
www.advmatinterfaces.de

Figure 5. Correlative APT and XANES characterization of the human bone–implant interface. a) HAADF-STEM image of the bone–implant interface. b) Optical density difference map ($OD_{400\ eV} - OD_{396\ eV}$) showing N-rich band. c) Color-coded map of three N-containing components: N-rich layer (blue), bone (green), and implant (red), derived from the fit of N-K edge stack to the N spectra in panel (e). The N-rich interfacial layer is also observed in the APT 3D reconstructions in panel (d) showing the atomic concentration of N and O. e) N-K edge XANES spectra from the N-rich layer, bone region and implant region, extracted from the regions indicated in panel (b).

commercial dental implant has been observed. Due to the different mechanical properties and biocompatibility of TiN compared to titanium dioxide, the introduction of TiN during machining should be considered during implant design.

In addition, the spectra of the C-K, Ti-$L_{2,3}$, and O-K edges were also investigated by STXM-XANES over the area displayed in Figure 5b. Different types of TiO_x signals are observed in the bone–implant interface region in both the Ti-$L_{2,3}$ and O-K edges. They are subtly different but reliably fit two separate regions distributed at the implant oxide layer: one region in connection with the bone, and the other directly adjacent to the implant surface (Figure S7, Supporting Information). This finding indicates the need for further investigation on the formation of these different phases of the oxide layer, in particular, to determine whether they are formed in vivo or during implant surface modification by laser. As for the spectra of C-K edge, two distinct C spectral signatures were found in the bone region, showing the existence of two species of C: carbonate and collagen (Figure S8, Supporting Information). However, the possible effects of electron beam damage in TEM and ion beam in FIB should be taken into consideration when analyzing the fine structures of C spectra.

3. Conclusions

This paper reports the first correlative 4D chemical tomography study of a bone–implant interface, including on-axis electron tomography, EELS tomography, and APT performed on the same sample. The combination of these methods reveals both nano- and atomic-scale information needed to understand biomineralization at the bone–implant interface. Based on morphological and chemical changes, observed by correlative 4D tomographic methods with supportive ELNES and XANES analyses, evidence for the existence of a transitional biointerphase at the bone–implant interface was demonstrated. On this particular laser-modified Ti dental implant, this intervening transition zone consisted of a disorganized apatite-rich material, which was identified as ACP immediately at the oxide surface by ELNES. In addition, the correlative APT analysis and spectroscopy characterizations provided new insights on the implant modification process and identified a TiN layer between the surface oxide and bulk metal of the commercial dental implant. Both findings have implications for the immediate and long-term osseointegration of dental implants. The correlative 4D tomographic workflow presented here for the bone–implant interface is applicable to other biological systems or materials science applications.

4. Experimental Section

Implant and Human Bone Interface Sample Preparation: The sample used in this study was from Biobank 513 at the University of Gothenburg, Sweden and was a dental implant (BioHelix, Brånemark Integration AB, Mölndal, Sweden) retrieved from a 66-year-old female patient after 47 months in service. This study was conducted under the ethical approval from the Hamilton Integrated Research Ethics Board at McMaster University. This screw-shaped commercial pure titanium dental implant was partly laser modified in the thread valleys via a Q-switched Nd:YAG laser (Rofin-Sinar Technologies Inc., Plymouth, USA) at an infrared wavelength of 1064 nm and spot size 100 μm, in ambient air. The implant with the surrounding human bone was fixed in formalin, dehydrated in a graded series of ethanol, embedded in plastic resin (LR White, London Resin Company, UK), and cut longitudinally for further study.

On-Axis Electron Tomography, EELS Tomography, and APT Sample Preparation: A dual-beam FIB instrument (Zeiss NVision 40, Carl Zeiss AG) equipped with a 30 kV gallium ion column, FEG SEM, carbon and tungsten gas injector system, and Kleindiek micromanipulator (Kleindiek Nanotechnik GmbH) was employed to prepare all TEM lamellae and needle-shaped samples for on-axis electron tomography, EELS tomography, and APT following published protocols.[40] A site of interest at the bone–implant interface was selected from the thread valleys where the implant was laser modified and was protected by a layer of tungsten deposition (10 μm x 2 μm x 0.5 μm). After rough milling of trenches, a wedge-shaped sample was lifted out and attached to the top of electropolished tungsten wires mounted in 1.8 mm copper tubes. The mounted wedge was annularly milled into needles to a final diameter of ≈200 nm using a 30 kV ion beam at successively lower currents (150–10 pA). A final low keV beam (10 kV, 80 pA) polishing step was performed to reduce surface damage and Ga ion implantation. After on-axis electron tomography, the needle-shaped sample was put back into the FIB and milled to 70 nm in diameter, which was suitable for both EELS tomography and APT using a low keV beam (10 kV, 80 pA). After the EELS tomography, FIB was also used to remove the surface C contamination using the same low beam of 10 kV and 80 pA.

On-Axis Electron Tomography Methods: The prepared needle of 200 nm diameter on the tungsten wire was mounted a Model 2050 on-axis rotation tomography holder (E.A. Fischione Instruments, Inc., Export, PA) and rotated through ±90° with an angular step size of 2° in the scanning transmission electron microscope (STEM) (Titan 80–300, operated at 300 kV). This tomographic tilt series was acquired using on a HAADF detector which provides Z contrast and by using FEI's Explore 3D software. The postacquisition image alignment via cross-correlation and reconstruction with simultaneous iterative reconstruction (SIRT, 20 iterations) were completed with the Inspect 3D (FEI Company, The Netherlands) software. The reconstructed volume was visualized via volume rendering and orthoslices using software Avizo (FEI Company, The Netherlands). The reconstructed volume was cropped by a custom MATLAB script (The MathWorks, Natick, MA).

EELS Tomography and ELNES Methods: A series of STEM-EELS spectrum images and corresponding dark-field images of the prepared 70 nm diameter needle were acquired in the tilt range ±70° with 2° tilt increment on an FEI Titan 80–300 microscope (FEI Company, Eindhoven, The Netherlands), operated at 300 kV. The microscope is equipped with a CEOS Probe Corrector, CEOS Image Corrector (CEOS GmbH, Heidelberg, Germany), and Gatan Quantum energy filter (Gatan Inc., Pleasanton, CA). The collection semiangle was 40 mrad and the probe current was ≈30 pA. The pixel size in the object plane was set to 1.56 nm, the exposure time for each pixel was 5 ms. The high-speed acquisition capability of the Quantum energy filter reduced acquisition time to about 2 min per spectrum image. Elemental distribution maps were extracted for Ca, C, Ti, and O from EELS spectrum images at every tilt angle using a power-law background model. For reconstruction, the alignment of the dark-field images was completed via cross-correlation by the software Inspect 3D (FEI Company, Eindhoven, The Netherlands) and the same shifts were applied to stacks of the chemical distribution

maps of each element. The reconstruction of all stacks was performed using Inspect 3D with SIRT (25 iterations). The reconstructed volumes were visualized using Amira. The reconstructed needle showed a shell of carbon contamination which accumulated on the needle's surface during data acquisition. In order to better visualize the carbon signal from the interior of the needle, the outside shell was removed by manually segmenting the needle surface and removing the outside carbon signal using a custom MATLAB script (The MathWorks, Natick, MA).

For ELNES, the spectrometer was set to an energy dispersion of 0.1 eV per channel to obtain the best energy resolution at the zero-loss peak (0.3 eV). The collection angle and convergence angle were 55 and 19 mrad, respectively. The collection aperture was 5 mm in radius and a dwell time of 0.015 s per pixel was used. Linear least-square fitting was used to remove background with a power law model.

APT Methods: This paper highlights two distinct APT datasets: Figure 1 and Figure 5d represent the same dataset for which correlative on-axis and EELS tomography is also shown, while Figure 3 is a different APT dataset from the same bone-implant specimen. Before APT, the needle-shaped samples were cleaned in the FIB and sputter coated with 15 nm of Ag, which appears outside of the field of view of the atom probe and therefore does not appear in the dataset. The atom probe experiments were conducted on a LEAP 4000XHR atom probe microscope (CAMECA Scientific Instruments, Madison, WI). A laser pulse ($\lambda = 355$ nm, 120 pJ, 100 kHz) was used to incite field evaporation from the sample with a base temperature of ≈43.4 K and the chamber pressure of 4.0×10^{-9} Pa. The evaporation rate was maintained around 0.005 ions per pulse (0.5%) by controlling the direct-current potential on the sample. Reconstruction and analysis was completed using the Integrated Visualization and Analysis Software package v3.6.8 (CAMECA Scientific Instruments, Madison, WI) assuming the shape was a hemispherical tip on a truncated cone. The reconstruction was spatially defined by assuming the tip radius to evolve as a function of a constant specimen shank angle. The input parameters for this algorithm of initial tip radius and specimen shank angle were obtained from STEM images of the sample, taken both before and after the APT experiment. This is critical for ensuring the accuracy of the reconstruction.

In order to minimize the interference of peak overlapping during mass spectra analysis and peaks assignment, the whole bone-Ti implant APT reconstructed volume was separated using 34 at% O isosurfaces, such that three subvolumes resulted: bone region (<34 at% O), oxide layer region (>34 at% O), and Ti implant region (<34 at% O). Separate ranging of these subvolumes helped clarify the identities of overlapping peaks. APT mass spectra (over 0–90 Da range) for each of these subvolumes are shown in Figure S3 (Supporting Information) and the ranged ion species are now listed in Table S1 (Supporting Information). STXM-XANES analysis: The soft X-ray spectromicroscopy beamline 10ID1 (SM)[58] at the Canadian Light Source (CLS, Saskatoon, SK, Canada) was used for the STXM-XANES study. STXM methodology has been described in detail previously.[32] Briefly, monochromated X-rays are focused to ≈30 nm by a Fresnel zone plate. The sample is positioned at the focal point and mechanically *x*–*y* raster scanned (1 ms per pixel) while recording the transmitted X-rays. Spectral data at the C-K, Ca-L$_{23}$, N-K, Ti-L$_{23}$, and O-K edges were collected by image sequences over the area displayed in Figure 5b. All data were analyzed by aXis2000.[59]

Supporting Information

Supporting Information is available from the Wiley Online Library or from the author.

Acknowledgements

Conflict of Interest

Keywords

[1] L. Addadi, S. Weiner, *Phys. Scr.* **2014**, *89*, 098003.
[2] U. G. K. Wegst, H. Bai, E. Saiz, A. P. Tomsia, R. O. Ritchie, *Nat. Mater.* **2014**, *14*, 23.
[3] W. Habraken, P. Habibovic, M. Epple, M. Bohner, *Mater. Today* **2016**, *19*, 69.
[4] F. Nudelman, A. J. Lausch, N. A. J. M. Sommerdijk, E. D. Sone, *J. Struct. Biol.* **2013**, *183*, 258.
[5] A. J. Lausch, B. D. Quan, J. W. Miklas, E. D. Sone, *Adv. Funct. Mater.* **2013**, *23*, 4906.
[6] D. E. Rodrigues, T. Thula-Mata, E. J. Toro, Y.-W. Yeh, C. Holt, L. S. Holliday, L. B. Gower, *Act Biomater.* **2014**, *10*, 494.
[7] K. Grandfield, *Phys. Today* **2015**, *68*, 40.
[8] P. I. Brånemark, U. Breine, R. Adell, B. O. Hansson, J. Lindström, A. Ohlsson, *Scand. J. Plast. Reconstr. Surg.* **1969**, *3*, 81.
[9] R. Brånemark, P. I. Brånemark, B. Rydevik, R. R. Myers, *J. Rehabil. Res. Dev.* **2001**, *38*, 175.
[10] M. Goutam, G. S. Chandu, S. K. Mishra, M. Singh, B. S. Tomar, *J. Orofacial Res.* **2013**, *3*, 197.
[11] Y. T. Sul, *Biomaterials* **2003**, *24*, 3893.
[12] J. E. Davies, V. C. Mendes, J. C. H. Ko, E. Ajami, *Biomaterials* **2014**, *35*, 25.
[13] J. E. Davies, *Biomaterials* **2007**, *28*, 5058.
[14] D. E. Steflik, A. L. Sisk, G. R. Parr, P. J. Hanes, F. Lake, M. J. Song, P. Brewer, R. V. McKinney, *J. Biomed. Mater Res.* **1992**, *26*, 529.
[15] M. M. Klinger, F. Rahemtulla, C. W. Prince, L. C. Lucas, J. E. Lemons, *Crit. Rev. Oral Biol. Med.* **1998**, *9*, 449.
[16] M. D. McKee, A. Nanci, *Microsc. Res. Tech.* **1996**, *33*, 141.
[17] J.-S. Kim, S.-M. Kang, K.-W. Seo, K.-Y. Nahm, K.-R. Chung, S.-H. Kim, J.-P. Ahn, *BioMed Res. Int.* **2015**, *2015*, 960410.
[18] A. Thorfve, A. Palmquist, K. Grandfield, *Mater. Sci. Technol.* **2015**, *31*, 174.

[19] K. Grandfield, S. Gustafsson, A. Palmquist, *Nanoscale* **2013**, *5*, 4302.
[20] G. Sundell, C. Dahlin, M. Andersson, M. Thuvander, *Acta Biomater.* **2016**, *48*, 445.
[21] J. Karlsson, G. Sundell, M. Thuvander, M. Andersson, *Nano Lett.* **2014**, *14*, 4220.
[22] K. Grandfield, A. Palmquist, H. Engqvist, *Philos. Trans. R. Soc., A* **2012**, *370*, 1337.
[23] G. Möbus, R. C. Doole, B. J. Inkson, *Ultramicroscopy* **2003**, *96*, 433.
[24] G. Haberfehlner, A. Orthacker, M. Albu, J. Li, G. Kothleitner, *Nanoscale* **2014**, *6*, 14563.
[25] P. Ercius, O. Alaidi, M. J. Rames, G. Ren, *Adv. Mater.* **2015**, *27*, 5638.
[26] T. F. Kelly, D. J. Larson, *Annu. Rev. Mater. Res.* **2012**, *42*, 1.
[27] A. Devaraj, D. E. Perea, J. Liu, L. M. Gordon, T. J. Prosa, P. Parikh, D. R. Diercks, S. Meher, R. P. Kolli, Y. S. Meng, S. Thevuthasan, *Int. Mater. Rev.* **2017**, *0*, 1.
[28] L. M. Gordon, D. Joester, *Nature* **2011**, *469*, 194.
[29] D. E. Perea, J. Liu, J. Bartrand, Q. Dicken, S. T. Thevuthasan, N. D. Browning, J. E. Evans, *Sci. Rep.* **2016**, *6*, 22321.
[30] L. M. Gordon, L. Tran, D. Joester, *ACS Nano* **2012**, *6*, 10667.
[31] B. Langelier, X. Wang, K. Grandfield, *Sci. Rep.* **2017**, *7*, 39958.
[32] A. P. Hitchcock, *Handbook of Nanoscopy*, Wiley-VCH, Weinheim, Germany **2012**, Ch. 22, pp. 745–791.
[33] G. Schmid, M. Obst, J. Wu, A. P. Hitchcock, *X-Ray Neutron Techniques for Nanomaterials Characterization*, Springer, Berlin **2016**, pp. 43–94.
[34] M. Obst, J. Wang, A. P. Hitchcock, *Geobiology* **2009**, *7*, 577.
[35] J. Cosmidis, K. Benzerara, *Biomineralization Sourcebook*, CRC Press, London, UK **2014**.
[36] J. Cosmidis, K. Benzerara, N. Nassif, T. Tyliszczak, F. Bourdelle, *Acta Biomater.* **2015**, *12*, 260.
[37] A. Devaraj, M. Gu, R. Colby, P. Yan, C. M. Wang, J. M. Zheng, J. Xiao, A. Genc, J. G. Zhang, I. Belharouak, D. Wang, K. Amine, S. Thevuthasan, *Nat. Commun.* **2015**, *6*, 8014.
[38] I. Arslan, E. A. Marquis, M. Homer, M. A. Hekmaty, N. C. Bartelt, *Ultramicroscopy* **2008**, *108*, 1579.
[39] A. E. Goode, A. E. Porter, M. P. Ryan, D. W. McComb, *Nanoscale* **2015**, *7*, 1534.
[40] X. Wang, F. A. Shah, A. Palmquist, K. Grandfield, *ACS Biomater. Sci. Eng.* **2017**, *3*, 49.
[41] R. F. Egerton, P. Li, M. Malac, *Micron* **2004**, *35*, 399.
[42] D. A. Bushinsky, K. L. Gavrilov, J. A. N. M. Chabala, R. Levi-setti, *J. Bone Miner. Res.* **2000**, *15*, 2026.
[43] G. Albano, M. Moor, S. Dolder, M. Siegrist, C. A. Wagner, J. Biber, N. Hernando, W. Hofstetter, O. Bonny, D. G. Fuster, *PLoS One* **2015**, *10*, 1.
[44] A. R. Irizarry, G. Yan, Q. Zeng, J. Lucchesi, M. J. Hamang, Y. L. Ma, J. X. Rong, *PLoS One* **2017**, *12*, e0175465.
[45] Y.-Y. Hu, A. Rawal, K. Schmidt-Rohr, *Proc. Natl. Acad. Sci. USA* **2010**, *107*, 22425.
[46] B. Xie, G. H. Nancollas, *Proc. Natl. Acad. Sci. USA* **2010**, *107*, 22369.
[47] N. Eliaz, N. Metoki, *Materials* **2017**, *10*, 334.
[48] V. Srot, B. Bussmann, U. Salzberger, C. T. Koch, P. A. van Aken, *Microsc. Microanal.* **2012**, *18*, 509.
[49] E. Beniash, R. A. Metzler, R. S. K. Lam, P. U. P. A. Gilbert, *J. Struct. Biol.* **2009**, *166*, 133.
[50] J. Mahamid, B. Aichmayer, E. Shimoni, R. Ziblat, C. Li, S. Siegel, O. Paris, P. Fratzl, S. Weiner, L. Addadi, *Proc. Natl. Acad. Sci. USA* **2010**, *107*, 6316.
[51] P. Lazar, J. Redinger, J. Strobl, R. Podloucky, B. Rashkova, G. Dehm, G. Kothleitner, S. Šturm, K. Kutschej, C. Mitterer, C. Scheu, *Anal. Bioanal. Chem.* **2008**, *390*, 1447.
[52] F. Hofer, P. Warbichler, A. Scott, R. Brydson, I. Galesic, B. Kolbesen, *J. Microsc.* **2001**, *204*, 166.

[53] M. McCracken, *J. Prosthodontics* **1999**, *8*, 40.

[54] Y. Zubavichus, M. Zharnikov, A. Schaporenko, M. Grunze, *J. Electron Spectros. Relat. Phenom.* **2004**, *134*, 25.

[55] J. Stewart-Ornstein, A. P. Hitchcock, D. H. Cruz, P. Henklein, J. Overhage, K. Hilpert, J. D. Hale, R. E. W. Hancock, *J. Phys. Chem. B* **2007**, *111*, 7691.

[56] B.-O. Aronsson, B. Hjörvarsson, L. Frauchiger, M. Taborelli, P.-H. Vallotton, P. Descouts, *J. Biomed. Mater. Res.* **2001**, *54*, 20.

[57] E. Conforto, D. Caillard, B.-O. Aronsson, P. Descouts, *Philos. Mag.* **2004**, *84*, 631.

[58] K. V. Kaznatcheev, C. Karunakaran, U. D. Lanke, S. G. Urquhart, M. Obst, A. P. Hitchcock, *Nucl. Instrum. Methods Phys. Res., Sect. A* **2007**, *582*, 96.

[59] A. P. Hitchcock, aXis2000 is written in Interactive Data Language (IDL), http://unicorn.mcmaster.ca/aXis2000.html (accessed: 2017).